



# On the nationwide variability of low-level jets prior to warm-season nocturnal rainfall in China revealed by radar wind profilers

Ning Li<sup>1,2,3</sup>, Jianping Guo<sup>1,4</sup>, Xiaoran Guo<sup>1,4</sup>, Tianmeng Chen<sup>1,4</sup>, Zhen Zhang<sup>1</sup>, Na Tang<sup>1</sup>, Yifei Wang<sup>1</sup>, Honglong Yang<sup>4</sup>, Yongguang Zheng<sup>3</sup>, and Yongshui Zhou<sup>5</sup>

<sup>1</sup>State Key Laboratory of Severe Weather Meteorological Science and Technology & Specialized Meteorological Support Technology Research Center, Chinese Academy of Meteorological Sciences, Beijing 100081, China

<sup>2</sup>College of Earth and Planetary Sciences, University of Chinese Academy of Sciences, Beijing 100049, China

<sup>3</sup>National Meteorological Centre, Beijing 100081, China

<sup>4</sup>CMA Field Scientific Experiment Base for Low-Altitude Economy Meteorological Support of Unmanned Aviation in Guangdong-Hong Kong-Macao Greater Bay Area, Shenzhen 518108, China

<sup>5</sup>Guizhou Meteorological Observatory, Guiyang 550001, China

**Correspondence:** Jianping Guo (jpguocams@gmail.com)

Received: 6 October 2025 – Discussion started: 16 October 2025

Revised: 24 February 2026 – Accepted: 26 February 2026 – Published: 4 March 2026

**Abstract.** Nocturnal rainfall initiation is closely linked to low-level jets (LLJs), but national-scale LLJ features over China – especially their evolution preceding warm-season nocturnal rainfall – remain unknown due to scarce high-resolution vertical observations. Here, we reveal the fine vertical structure of LLJs and their rapid evolution within 2 h preceding the onset of nocturnal heavy rain (HR) and non-HR across four phases of rainy seasons in China during the warm season (April–October) of 2023–2024, utilizing data from a nationwide network of radar wind profilers (RWPs) in combination with surface observations and reanalysis data. Results show that nocturnal rainfall accounted for over 50 % of warm-season rainfall, with 56 % preceded by LLJs within 2 h of its onset. In monsoon regions, ~ 45 % of nocturnal HR were LLJ-associated (LLJ\_HR), producing heavier rainfall than non-LLJ\_HR events. Critically, LLJ\_HR events underwent a minute-scale “rapid reorganization” of the LLJ structure, characterized by oscillatory evolution in jet height, frequency and strength. This creates a favorable environment for the “final-stage intensification” of dynamic field during the last ~ 30 min, where widespread intensification of jet – coupled with significant thermodynamic instability – acts as a primary dynamical forcing mechanism and a key precursor signal for HR initiation. In stark contrast, LLJ\_non-HR events exhibited quasi-steady or weakening dynamical trends, accompanied by an inadequate thermodynamic response that lacks such synergistic coupling. These findings demonstrate that minute-scale dynamic adjustments driven by swift evolution of the LLJ are essential for nocturnal HR, offering critical observational constraints for regional model parameterizations and nowcasting accuracy.

## 1 Introduction

Forecasting nocturnal heavy rainfall (HR) and associated severe convective weather remains a major challenge in hazardous weather prediction (Davis et al., 2003; Trier et al., 2006), owing to the complexity of triggering mechanisms, the scarcity of continuous high-resolution observations, and inaccuracies in model parameterizations (Carbone and Tuttle, 2008; Reif and Bluestein, 2017; Weckwerth et al., 2019). Crucially, the low-level jet (LLJ) that exhibit a diurnal cycle with a maximum at night is widely recognized as a key contributor to nocturnal HR (Bonner, 1968; Mitchell et al., 1995; Tuttle and Davis, 2006), as documented in regions or countries such as the Great Plains of the United States (Maddox, 1983; Higgins et al., 1997), Argentina (Marengo et al., 2004), India (Monaghan et al., 2010), North China Plain (Li et al., 2024).

The LLJs primarily originate from the inertial oscillations (IO) following the sudden decay of turbulence after sunset (Blackadar, 1957) and thermal imbalances induced baroclinicity over sloping terrain (Holton, 1967). Functioning as concentrated corridors for heat, moisture, and momentum transport, LLJs can modulate the diurnal oscillation in water vapor by IO (Rasmusson, 1967; Zhang et al., 2019) and enhance convective instability, particularly when elevated high- $\theta_e$  air encounters frontal boundaries (Trier et al., 2017). Also, strong low-level vertical wind shear (VWS) associated with LLJs necessarily benefits deep lifting (Maddox et al., 1982; Stensrud, 1996; Rasmussen and Houze, 2016). These mechanisms collectively provide essential thermodynamic and dynamic support for the initiation and organization of nocturnal convection, especially where LLJs force low-level ascent at jet termini or via positive vorticity advection left of the jet axis (Chen et al., 2017; Du and Chen, 2019; Xia and Zhao, 2009).

Furthermore, LLJs interact synergistically with other key factors to trigger HR that is associated with mesoscale convective systems (Chen et al., 2010, 2017, 2024), including terrain effects (Anthes et al., 1982; Pan and Chen, 2019; Huang et al., 2020), gravity waves (Weckwerth and Wakimoto, 1992), among others. These interactions are highly sensitive to the prevailing synoptic and subsynoptic-scale environmental conditions (e.g., Hodges and Pu, 2019) and fine-scale structural of LLJs, including LLJ frequency, spatial redistribution, and particularly localized wind profile accelerations (Pitchford and London, 1962; Walters et al., 2008; Du and Chen, 2019; Li et al., 2024). Understanding these intricate evolution features of LLJs is critical for improving the forecasting of nocturnal HR.

Despite advances facilitated by regional reanalysis (e.g., Doubler et al., 2015; Li and Du, 2021), numerical modeling (e.g., Zhang and Meng, 2019), radiosonde observations (e.g., Whiteman et al., 1997; Yan et al., 2021), and emerging artificial intelligence techniques (e.g., Subrahmayam et al., 2024) in understanding the climatology and physical mechanisms

of LLJs and their role in HR forecasting, significant knowledge gaps remain. The insufficient spatiotemporal resolution of conventional observing systems limits the ability to capture rapid pre-storm environmental changes (Weisman et al., 2015; Cao et al., 2025; Roots et al., 2025), thereby hindering systematic analysis of the fine-scale structure of LLJs and their minute-scale evolution within the critical 2-h window preceding rainfall.

Moreover, the mechanisms and impacts of LLJs exhibit considerable variation across monsoon phases and geographic regions. As a classic monsoon climate region, China exhibits particularly prominent nocturnal rainfall contributions across major climate-sensitive areas (Yu et al., 2014), where LLJs play a crucial role in modulating primary rainfall belts (Sun, 1986; Chen et al., 2010; Wang et al., 2013; Hironouchi et al., 2019), such as those in Eastern China (Chen et al., 2017; Xue et al., 2018) and South China (Du et al., 2020; Bai et al., 2021; Dong et al., 2021). However, nationwide comparative studies examining LLJ precursor signals across different monsoon phases in China are still lacking.

Radar wind profilers (RWPs) can offer transformative potential by capturing minute-resolution wind profiles to reveal pre-rainfall dynamic precursors (Zamora et al., 1987; Du et al., 2012; Molod et al., 2019; Guo et al., 2023). For example, Gebauer et al. (2018) demonstrated the capability of RWPs to elucidate how heterogeneous structures of LLJ trigger nocturnal convection in Great Plains; Based on a linear net of RWPs deployed across the North China Plain, our previous study (Li et al., 2024) observed rapid intensification of moisture flux convergence (MFC) driven by a surge in LLJs profile within 30 min preceding nocturnal rainfall onset, highlighting the sensitivity of RWP to minute-scale perturbations of LLJs profiles. However, it remains an open question whether this minute-scale precursor is universally applicable across diverse monsoon phases throughout mainland China. Furthermore, the systematic differences in the fine-scale LLJ evolution that distinguish HR from non-HR have yet to be fully elucidated.

Therefore, this study utilizes a nationwide network of RWPs to address the following two questions: (1) How do the vertical structure of LLJs and their minute-scale evolution within 0–2 h preceding nocturnal rainfall vary across different rainy season phases? and (2) What are the systematic differences in LLJ dynamic-thermodynamic mechanisms between LLJ-influenced HR and non-HR events? The remainder of this paper is structured as follows: Sect. 2 details data and methodology, Sect. 3 presents comparative analyses of characteristics of rainfall and LLJs evolution, and Sect. 4 synthesizes key conclusions.

## 2 Data and Methodology

### 2.1 Radar wind profiler measurements

The RWP observations collected from 31 stations across China (Fig. 1) from April to October in 2023–2024 were analyzed in this study, which can provide wind speed and direction with a vertical resolution of 120 m and an interval of 6 min (Liu et al., 2019). To reduce the potential influence of poor data quality, RWP data underwent strict quality control following procedures proposed by Wei et al. (2014) and Miao et al. (2018). Firstly, to minimize contamination from precipitation particles, which can introduce significant errors in Doppler-based wind retrieval, all observations during rainfall periods were removed. Secondly, within each profile below 3 km above ground level (a.g.l.), missing values and significant outliers that were defined as values exceeding 2.5 standard deviations from the mean were removed. Next, for each profile, if more than 40 % of the data points below 3 km a.g.l. were outliers or missing, that entire profile was discarded. Finally, discontinuous, or missing data points were estimated using linear interpolation. Following this quality control process, 109 400 wind profiles were discarded and a total of 2 606 042 profiles across China were available for analysis during the study period.

### 2.2 Multi-source meteorological data

In addition, 1-min rainfall measurements were directly acquired from the rain gauge measurements at 2160 national weather stations across China to identify rainfall events. Rainfall amounts were accumulated over 6-min intervals to ensure temporal alignment with the RWP measurements. Ground-based meteorological variables are measured at 1-min intervals from national weather stations, including 2-m air temperature, relative humidity, and surface pressure. All ground-based data have undergone rigorous quality control (China Meteorological Administration, 2020; Zhao et al., 2024) and are publicly accessible at the National Meteorological Information Center of China Meteorological Administration (CMA).

Furthermore, to diagnose large-scale circulation patterns and environmental conditions preceding nocturnal rainfall influenced by LLJs, this study utilized meteorological variables derived from the fifth generation of the European Centre for Medium-Range Weather Forecasts atmospheric reanalysis (ERA5) of the global climate (Hersbach et al., 2023). The ERA5 data features a horizontal resolution of  $0.25^\circ \times 0.25^\circ$  across 37 vertical pressure levels and hourly temporal resolution. Unless otherwise specified, all datasets cover the study period of April to October in 2023–2024.

### 2.3 Identification of nocturnal rainfall events

Firstly, days with typhoon activity were excluded. To minimize the impact of rainfall on RWP measurements, a min-

imum dry interval of 2 h was required between consecutive rainfall events. Following the methodology of Li et al. (2024), a rainfall occurrence was defined when the accumulated rainfall measured by all rain gauges within a 25-km radius of each RWP station exceeded 0.1 mm. To account for rainfall intermittency and filter out transient noise, a valid rainfall event required the initial detection to be followed by at least two subsequent occurrences within 30 min. Any isolated initial occurrence not meeting this criterion was discarded. Notably, this 25-km radius serves as a rigorous spatial constraint to not only mitigates the limitations of single-gauge measurements but also ensures the onset of rainfall at this scale are temporally coherent with that of the rain gauge co-located with RWP (as confirmed by sensitivity tests in Fig. S1 and Table S1 in the Supplement). This guarantees direct physical coupling between local rainfall and the RWP-observed wind profiles.

Nocturnal rainfall events were defined as those occurring between 20:00 and 08:00 Local Standard Time (LST). Based on operational classifications from the National Water Resources Bureau and CMA, the rainy season was categorized into four consecutive phases: (1) the South China Pre-summer Rainy Season (1 April–8 June 2023 and 1 April–9 June 2024), (2) the Meiyu Season (9 June–14 July 2023 and 10 June–21 July 2024), (3) the North China Rainy Season (15 July–31 August 2023 and 22 July–31 August 2024), and (4) the West China Autumn Rainy Season (1 September–31 October for both 2023 and 2024). These phases are subsequently designated as Phase 1 to Phase 4 throughout this study. Four regions of interest (ROIs) were subsequently selected for detailed analysis (see Table 1).

Further screening identified locally nocturnal HR events, where the mean 6-min rainfall intensity exceeded the 75th percentile of all recorded rainfall events at each station. This threshold can effectively distinguish significant HR from weak rainfall while ensuring a sufficient sample size for robust statistical analysis of minute-scale LLJ dynamics (Table S1). Furthermore, a sensitivity test by varying the thresholds to 85th and 95th percentile to ensure that the main conclusion regarding the precursory signals of LLJs is robust within a reasonable threshold range (see Figs. S2–S5).

Statistical analysis revealed 3155 nocturnal rainfall events during the 2023–2024 warm seasons (within the 31 red circles shown in Fig. 1). Event counts per rainy season phase were 1109, 689, 652, and 705 respectively, with 841 events classified as nocturnal HR events.

### 2.4 Identification of LLJs and associated rainfall event

To ensure identified LLJs exhibit significant vertical wind shear characteristic of jet-like profiles, the following criteria are adopted: (1) a maximum horizontal wind speed exceeding  $10 \text{ m s}^{-1}$  in the lowest 3 km a.g.l., and (2) a wind speed reduction of at least  $3 \text{ m s}^{-1}$  from the maximum to minimum below 3 km a.g.l., or to 3 km a.g.l. if no minimum

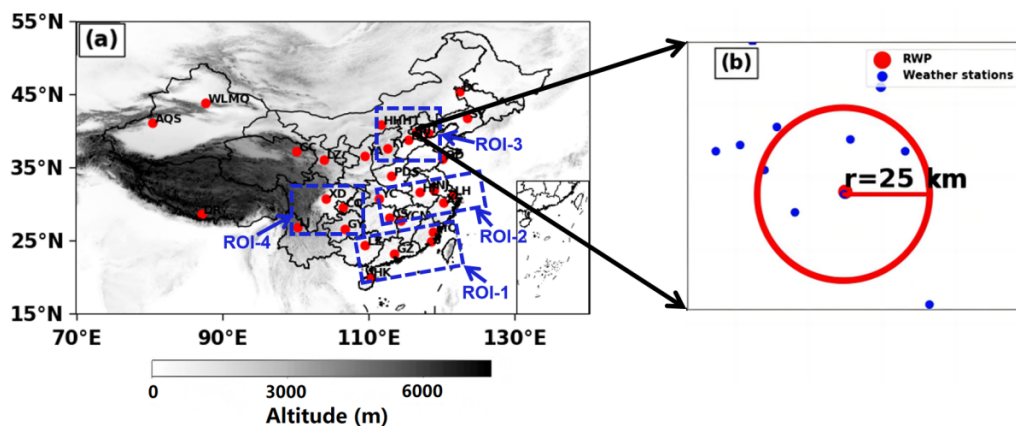


**Figure 1.** (a) Spatial distribution of 31 Radar Wind Profiler (RWP) stations (red dots) across China, with four regions of interest (ROIs) demarcated by blue dashed boxes: ROI-1, ROI-2, ROI-3, and ROI-4. (b) Schematic of spatial co-location: Beijing Observatory's RWP (red circle) and rain gauges (blue dots) within a 25-km radius.

**Table 1.** Table of Representative Radar Wind Profiler Stations in Mainland China.

Region	Station	Longitude (°)	Latitude (°)	Altitude (m)
ROI-1	58839 MQ	118.86	26.22	160.70
	59046 LZ	109.46	24.36	314.40
	59137 JJ	118.54	24.81	124.80
	59287 GZ	113.48	23.21	65.00
	59758 HK	110.25	19.99	69.00
ROI-2	57461 YC	111.36	30.74	253.80
	57687 CS	112.79	28.11	119.00
	57793 YCN	114.36	27.79	132.00
	58238 BJ	118.90	31.93	40.60
	58321 HF	117.03	31.57	50.00
	58367 LH	121.47	31.18	5.00
	58459 XS	120.29	30.18	48.80
ROI-3	53463 HHHT	111.68	40.82	1152.10
	53772 TY	112.58	37.62	785.00
	54511 BJ	116.47	39.81	31.50
	54534 TS	118.10	39.65	23.20
	54602 BD	115.48	38.73	16.80
ROI-4	57816 GY	106.73	26.59	1197.60
	56290 XD	104.18	30.77	514.00
	56651 LJ	100.22	26.85	2382.40
Other stations	50936 BC	122.47	45.36	156.00
	51463 WLMQ	87.65	43.79	935.00
	51628 AKS	80.38	41.12	1107.10
	52754 GC	100.08	37.2	3301.50
	52889 LZ	103.89	36.06	1519.20
	57516 CQ	106.46	29.57	260.00
	53845 YA	109.45	36.58	1180.40
	54342 SY	123.51	41.73	50.00
	54857 QD	120.13	36.23	12.00
	55664 DR	87.07	28.63	4302.00
	57171 PDS	113.12	33.77	142.00

exists. These deliberately conservative wind speed thresholds maximize LLJ sample size for enhanced statistical robustness. This definition standard has been widely adopted in previous studies (Bonner, 1968; Whiteman et al., 1997; Du et al., 2014; Yan et al., 2021). The strength of LLJ or jet nose is defined as the maximum wind speed along the entire profile. The LLJ core height is defined as the altitude of the wind speed maximum during LLJ occurrences. Correspondingly, the LLJ direction is determined by the wind direction at the height of the LLJ.

We define rainfall events where LLJ occurs at least twice within 2 h before rainfall as an LLJ event (Li et al., 2024). The HR events influenced by LLJs (LLJ\_HR events), HR events without LLJ influence (non-LLJ\_HR events), and non-HR events affected by LLJ (LLJ\_non-HR events) are further distinguished.

### 3 Results and discussion

#### 3.1 General characteristics of nocturnal rainfall and LLJs

Firstly, we characterized the spatiotemporal patterns of rainfall and LLJs observed nationwide during the 2023–2024 warm season. Nationally, nocturnal rainfall accounted for 50.9 % of total warm-season rainfall, with pronounced concentrations over North, Northeast and Southwest China (Fig. 2d and 2g). In contrast, the pronounced daytime rainfall dominance in South China (Fig. 2a) may arise from the interaction between enhanced onshore monsoonal flows and terrain (Bai et al., 2021), sea breeze fronts and cold pool (Chen et al., 2016). In terms of frequency, nocturnal rainfall occurred more frequently, constituting 52.5 % of the total rainfall frequency versus 47.5 % for the daytime, with the highest nocturnal proportions found in southwestern and eastern regions (Fig. 2e and h). Although the national mean rainfall intensity was generally lower at night ( $1.2 \text{ mm h}^{-1}$ ) than during the day ( $1.8 \text{ mm h}^{-1}$ ; Fig. 2c and f), the probability of nocturnal HR occurrence was significant (51.3 %), particularly across western, northern, and northeastern China (Fig. 2i).

Figure 3 displays the key attributes of LLJs detected at all 31 RWPs across China using the criteria defined in Sect. 2. Nocturnal LLJ activity occurred more frequently, with an overall occurrence frequency increase of nearly 18 % relative to diurnal LLJs (Fig. 3a and e). This pronounced nighttime enhancement is consistent with the classical IO mechanism, whereby reduced surface friction after sunset allows the decoupled boundary layer to accelerate and form stronger LLJs. Spatially, both daytime and nighttime LLJs were more prevalent in eastern and southeastern China, particularly along the Yangtze River basin and coastal regions, where moisture-rich monsoonal flows dominate. In contrast, lower frequencies were observed over northwestern China, likely reflecting weaker large-scale moisture transport and reduced baroclinicity in arid inland regions.

In terms of jet core height (Fig. 3b and f), nocturnal LLJs generally exhibited slightly lower core altitudes compared to their daytime counterparts, with most cores concentrated below  $\sim 1500 \text{ m}$ . This lowering of the jet core at night is consistent with boundary-layer stabilization and the formation of a shallow nocturnal inversion, which confines the jet maximum to lower altitudes. Regarding jet intensity (Fig. 3c and g), nighttime LLJs were typically stronger, with a higher proportion of stations reporting wind speeds exceeding  $16\text{--}18 \text{ m s}^{-1}$ . The combination of enhanced wind speed and reduced core height suggests a more concentrated and dynamically organized jet structure during nighttime hours. The dominant wind directions (Fig. 3d and h) further reflect regional circulation controls. Southeasterly and southwesterly LLJs prevailed in eastern China, consistent with the transport of warm, moist air from the South China Sea and western Pacific during the warm season. In northern and northwestern regions, LLJs exhibited more variable directional characteristics, likely influenced by synoptic-scale pressure gradients and topographic channeling effects.

Overall, Fig. 3 demonstrates that nocturnal LLJs are not only more frequent but also stronger and lower in altitude than their daytime counterparts. These structural differences imply enhanced moisture transport efficiency and greater potential for nighttime convective organization, providing a dynamical foundation for the observed diurnal asymmetry in heavy rainfall occurrence examined in subsequent sections.

Statistical analysis revealed a substantial linkage between LLJs and nocturnal rainfall. Specifically, 56 % of all nocturnal rainfall events across China were preceded by the presence of LLJs within 2 h, establishing nocturnal rainfall influenced by LLJs as a major component of warm-season rainfall in China. This relationship was strongly modulated by the seasonal migration of the western Pacific subtropical high (WPSH), whose northward progression and subsequent retreat governed the latitudinal displacement of HR belts and closely synchronized with the spatiotemporal evolution of LLJ activity. The proportion of nocturnal rainfall events associated with LLJs during the four rainy season phases reached 60.4 %, 56.3 %, 49.4 %, and 54.9 %, respectively (solid-filled bars in Fig. 4a). Among 841 identified nocturnal HR events nationwide, 33.9 %–47.2 % were classified as LLJ\_HR events across the four phases (diagonally striped bars in Fig. 4a). This contrast between the high LLJ association for general nocturnal rainfall and the more moderate fraction for HR indicates that, although LLJs are a frequent precursor to rainfall, their presence alone does not guarantee the occurrence of heavy rainfall.

A more detailed statistical analysis of ROIs revealed the key role of LLJ coupling in primary rain belt regions of each phase. A total of 71, 49, 33, and 34 nocturnal HR events were identified in these ROIs during the period from Phase 1 to Phase 4 (Fig. 4b). On average, nearly 45.0 % of HR events in these regions were associated with LLJs within 2 h before onset. Spatial analysis further confirmed that these LLJ\_HR

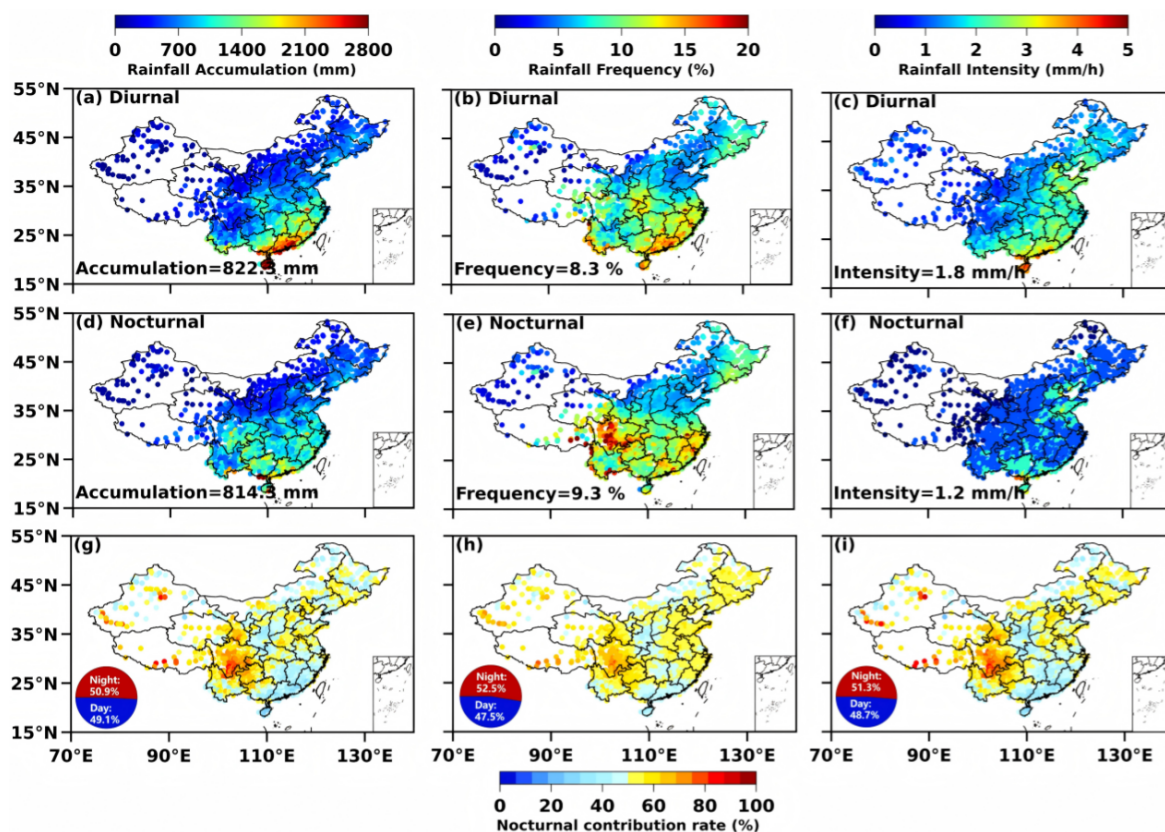


**Figure 2.** (a–c) Spatial distributions of accumulated rainfall (mm), rainfall frequency (%) and rainfall intensity ( $\text{mm h}^{-1}$ ) in the daytime from April to October in 2023–2024. The numbers in the upper left corner represent the national average; (d–f) the same as (a–c), but in the nighttime; (g–i) Nocturnal contribution ratios of accumulated rainfall, frequency, and occurrence frequency of heavy rainfall (> 75th percentile intensity). The pie charts illustrate the relative contribution rates of daytime (blue) and nighttime (red) at the national scale.

events consistently produced heavier rainfall intensities than non-LLJ\_HR events (red boxes in Fig. 5), particularly within the four ROIs (red boxes in Fig. 5). Nevertheless, the non-LLJ\_HR events exhibited spatially heterogeneous intensity distributions, where localized maxima may occur in areas outside the primary rain belts. For instance, during Phase 2 in ROI-3 (Fig. 5f), sporadic high-intensity events driven by deep cold trough system resulted in high site-averaged intensities even without LLJs, whereas in ROI-2, the absence of LLJs typically corresponded to weaker frontal precipitation (Fig. S6).

Furthermore, at the national scale, probability distributions of rainfall intensity (Fig. 6) indicated that LLJ\_HR events exhibited a significantly higher tail ( $\geq 2.0 \text{ mm } 6 \text{ min}^{-1}$ ) compared to non-LLJ\_HR events during Phases 1 and 3. During Phases 2 and 4, however, the distributions of the two event types were comparable, with LLJ\_HR events showing slightly weaker intensities. Regionally, rainfall intensities within the key ROIs generally exceeded the national average, particularly for LLJ\_HR events. Specifically, ROI-1 and ROI-2 demonstrated significantly higher probabilities of heavier rainfall ( $\geq 2.0 \text{ mm } 6 \text{ min}^{-1}$ ) in LLJ\_HR events. No-

tably, LLJ\_HR events in ROI-4 favored intensities near 0.5 and  $2.8 \text{ mm } 6 \text{ min}^{-1}$ , yet the overall probabilities of heavier rainfall remained slightly lower than non-LLJ\_HR events. Despite the relatively high frequency of LLJ\_HR events in ROI-3 during Phase 3 (see the pie charts in Fig. 6), their probability of producing heavier rainfall was comparable to – rather than substantially greater than – that of non-LLJ\_HR events. Moreover, this region exhibited the sharpest decay in probability density for heavier rainfall among all regions. This behavior suggests that, although LLJs occur frequently in this region and season, their contribution to extreme rainfall intensity is not dominant. Instead, other non-LLJ forcing mechanisms, such as topographic lifting and mesoscale convective systems, may play an equally or more significant role in generating HR in ROI-3 during Phase 3.

In summary, although LLJ\_HR events were generally associated with enhanced rainfall intensities across most ROIs and most phases, only  $\sim 31.1\%$  of all identified LLJ events were ultimately classified as HR events (Fig. 4b). This relatively low conversion rate indicates that the mere presence of LLJs is not sufficient to produce HR. The substantial number of LLJ\_non-HR events implies that additional dynamic and

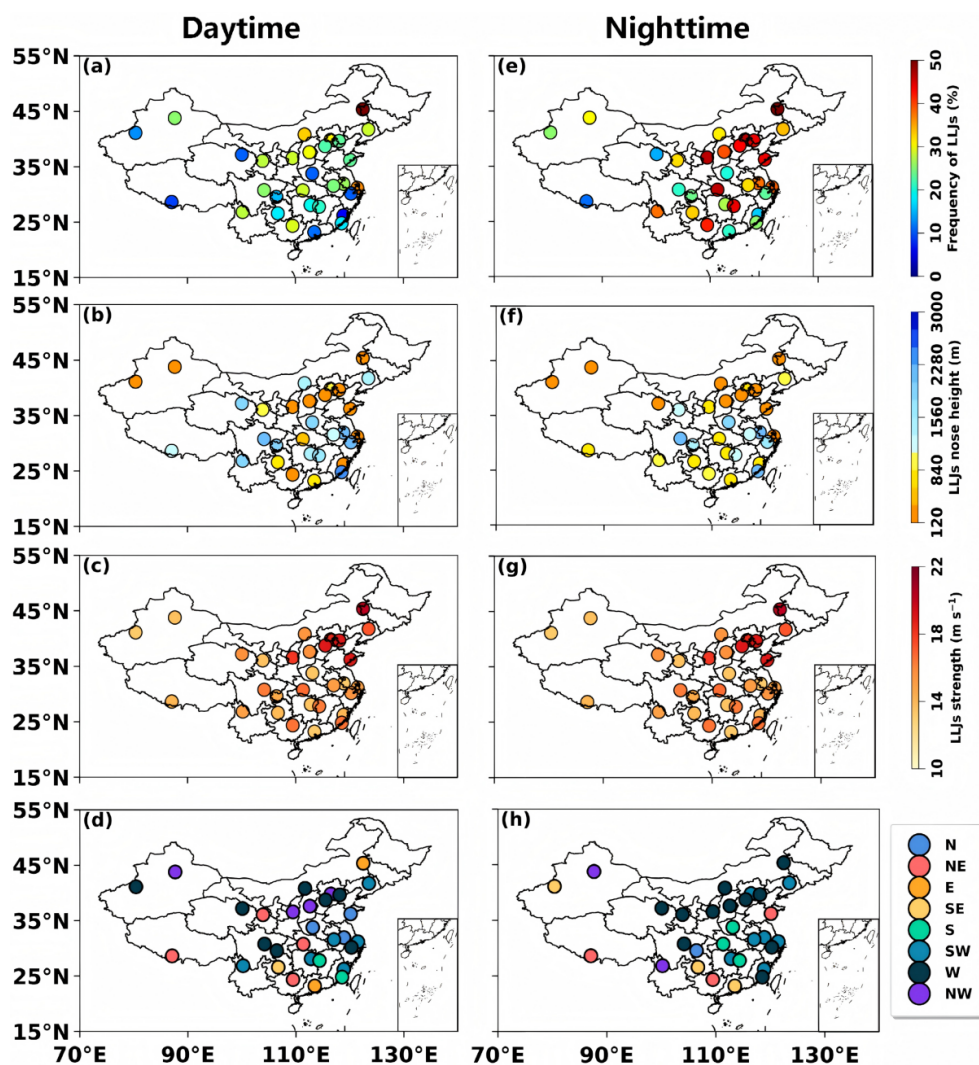


**Figure 3.** (a–d) Spatial distribution of occurrence frequency, height, strength, and the dominant wind direction of LLJs observed by 31 RWP stations during April–October from 2023 to 2024 in the daytime. (e–h) Same as (a–d), but in the nighttime.

thermodynamic conditions must coexist with LLJs to trigger HR. In particular, factors such as moisture transport efficiency, vertical wind shear configuration, atmospheric stability, and mesoscale lifting mechanisms may modulate whether an LLJ evolves into a heavy-rain-producing system. Therefore, a detailed further examination of the fine-scale vertical structures of LLJs prior to rainfall onset is crucial to disentangle the dynamical characteristics that distinguish HR-producing LLJs from non-HR cases, as explored in the following sections.

### 3.2 Minute-scale evolution of LLJs preceding nocturnal heavy and non-heavy rainfall

To elucidate the contrasting precursor characteristics of LLJs that lead to nocturnal rainfall of differing intensities, this section examines fine-scale vertical structure and continuous

evolution of LLJs within 2 h preceding both LLJ\_HR and LLJ\_non-HR events during four phases in their respective ROIs. The results revealed the distinct spatiotemporal variations in vertical structure and evolutionary patterns of LLJs occurred across seasonal phases.

During Phase1 in ROI-1, LLJ\_HR events exhibited a significant increase in frequency starting 108 min before rainfall onset, reaching secondary peaks at  $-84$  and  $-60$  min, culminating in maximum frequency immediately preceding HR (Fig. 7a). Meanwhile, the average wind profiles showed a rapid intensify trend from 48 min before HR onset, with the jet core reaching its peak wind speed (about  $12.2 \text{ m s}^{-1}$ ) and its height distinctly decreased (Fig. 8a), although there is the transient weakening of jet strength within 60–48 min preceding HR. These LLJs featured a bimodal vertical distribution with frequent occurrence layers at 0.5–1 km and 1.5–2 km a.g.l. This structure was characteristic of

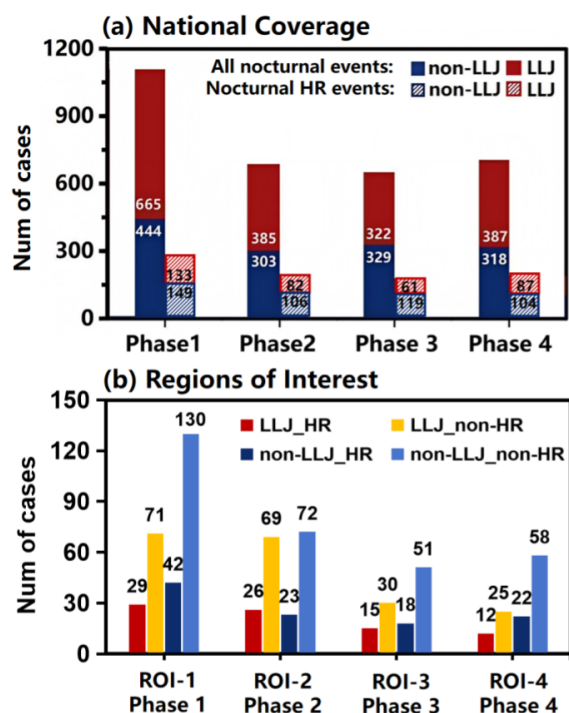


**Figure 4.** (a) Statistics of all nocturnal rainfall events (solid-filled bars) and nocturnal heavy rainfall (HR; diagonally striped bars) events across China during four phases, categorized into LLJ events (red) and non-LLJ events (blue). (b) Statistics of nocturnal rainfall events within the four ROIs (ROI-1 to ROI-4) during their corresponding phases, categorized into four types: LLJ\_HR (red), LLJ\_non-HR (yellow), non-LLJ\_HR (dark blue), and non-LLJ\_non-HR (light blue) events.

double low-level jets (DLLJs), where the coexistence of the boundary layer jets (BLJs) and synoptic-system-related jets (SLLJs) generated a deep layer of forced ascent via BLJ-exit convergence and SLLJ-entrance divergence. This dynamical coupling significantly favors organized deep convection in ROI-1 (Uccellini and Johnson, 1979; Du and Chen, 2018, 2019; Liu et al., 2020). Note that the composite wind profile (Fig. 8a) does not show a distinct bimodal vertical distribution due to smoothing from averaging. Detailed examination of wind profiles revealed that approximately 40 % of LLJ\_HR events exhibited DLLJs, while only 20 % of LLJ\_non-HR events showed such a structure. Therefore, LLJ\_non-HR events lacked this dynamic coupling, with jets predominantly confined to the single 0.5–1 km layer. Although LLJ\_non-HR events showed a gradual increase in frequency from –48 min, along with strengthening winds prior to rainfall (Figs. 7e and 8e), these changes were rather limited compared to the pronounced evolution seen in LLJ\_HR events under a background of overall lower frequency and weaker intensity. This steady and weak dynamical structure failed to provide sufficient dynamic lifting to efficiently initiate strong convection.

Both event types exhibited notably high frequencies and intensities of LLJs over ROI-2 during Phase 2, yet their evolutionary dynamics diverged sharply. For LLJ\_HR events, a coherent oscillatory vertical reorganization of LLJs is evident (Figs. 7b and 8b). At the first stage, both LLJ frequency and wind speed maximum peaked (exceeding  $12 \text{ m s}^{-1}$ ) at –120 min, with the core situated 1.5–2 km a.g.l. Subsequently, a rapid descent of frequently occurring height of LLJs to below 1 km a.g.l., occurred, accompanied by a concurrent decline in frequency and profile intensity to a minimum around 84–72 min preceding HR. Analysis of wind kinetic energy and its vertical transport (see Eqs. 1 and 2 in the Supplement) confirmed that the “sudden drop” likely results from the downward momentum transfer (Fig. S7a and c), which can efficiently enhance low-level disturbances and dynamic forcing and serve as an effective indicator of HR 1–2 h later (Liu et al., 2003; Fu et al., 2020). Following this descent, a distinct recovery phase ensued from –60 min, where the frequency increased reaching a secondary peak at –48 min and jet core re-ascended to 1–2 km a.g.l. The LLJ profile strength re-intensified to about  $11.4 \text{ m s}^{-1}$ . This rise of the jet core and secondary enhancement are likely tied to cold pool-LLJ interactions and intensified upward motion or latent heat release in convective clouds (further discussed in Sect. 3.3). In conclusion, this pattern suggests an intense internal dynamical adjustment process. In comparison, LLJ\_non-HR events lacked such low-level momentum transfer signals (Fig. S7b and d) and maintained a quasi-steady state, with consistent LLJs strength (near  $11.8 \text{ m s}^{-1}$ ) and a preferred height range of 1–2 km a.g.l. (Fig. 8f). The LLJs frequency exhibited gradual changes, peaking weakly at 36 min preceding rainfall before a subsequent rapid decrease (Fig. 7f). This pattern indicates an absence of the rapid dynamical redistribution observed in LLJ\_non-HR events.

During Phase 3 in ROI-3, LLJ\_HR events exhibited a bimodal temporal distribution in LLJ frequency, with prominent peaks at –96 and –48 min (Fig. 7c). The dominant LLJ height was centered between 1–1.5 km a.g.l. The wind profiles showed a corresponding evolution where the maximum wind speed increased from approximately  $8.0 \text{ m s}^{-1}$  at –120 min to a first peak about  $9.5 \text{ m s}^{-1}$  by –84 min. Following a transient weakening (–48 to –24 min), a secondary intensification occurred immediately preceding HR onset (Fig. 8c). Conversely, LLJ\_non-HR events were characterized by substantially lower LLJs frequency (around 20 %) and a more diffuse structure (Fig. 7g), with wind profiles exhibiting weaker intensification preceding rainfall (Fig. 8g). Consequently, the rapid reorganization and final intensification of LLJs appeared to be critical dynamical drivers for HR. However, despite the potential influences of regional thermodynamics and topography, the insufficient dynamical forcing from overall weaker wind profiles in ROI-3 remained the primary reason for its comparatively lower probability of heavier rainfall ( $\geq 2.0 \text{ mm } 6 \text{ min}^{-1}$ ).

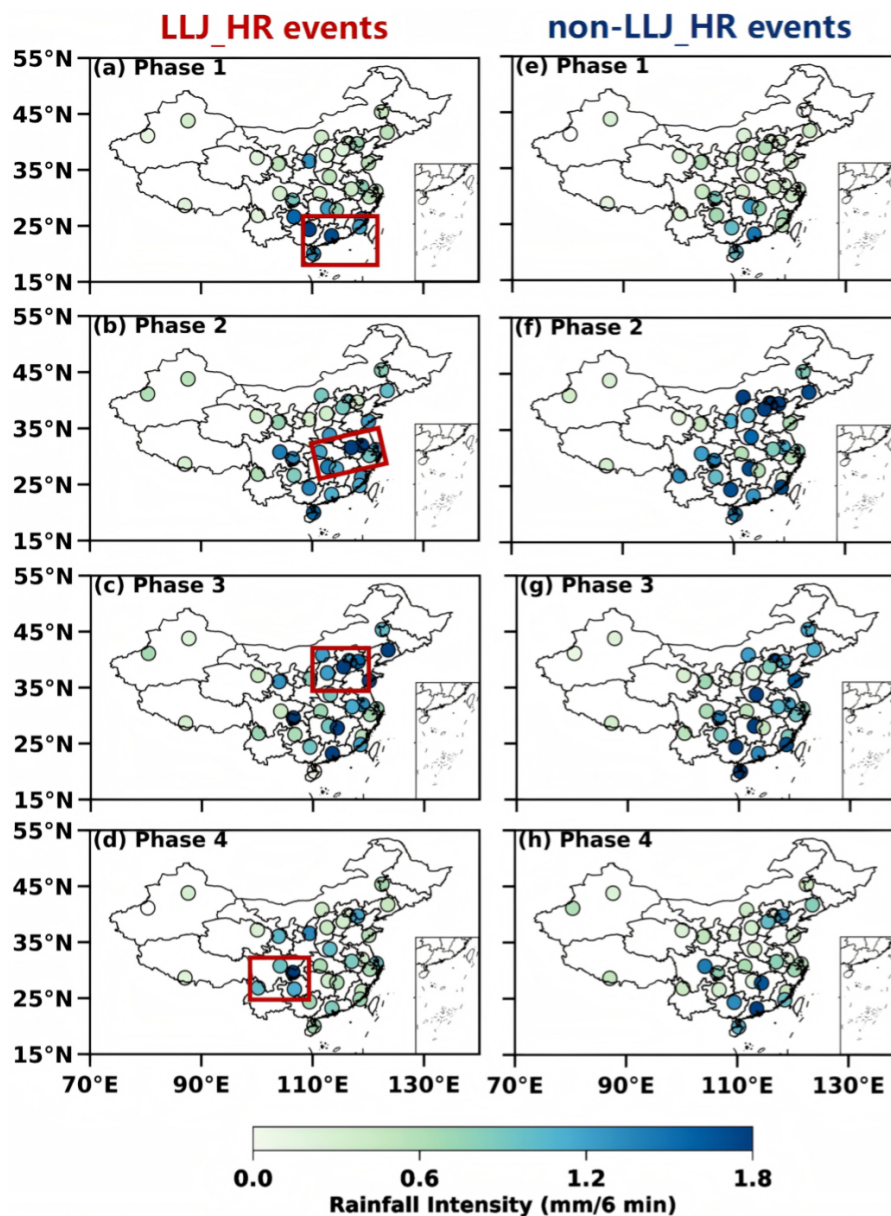


**Figure 5.** (a–d) Spatial distributions of site-averaged rain rate ( $\text{mm } 6 \text{ min}^{-1}$ ) for nocturnal LLJ\_HR events during the warm season from Phase 1 to Phase 4 across China; (e–h) Same as (a–d), but for non-LLJ\_HR events. The red frame indicates four ROIs.

During Phase 4 in ROI-4, LLJ\_HR events exhibited a distinctive two-stage intensification process. The wind profiles initially strengthened rapidly starting from  $-120 \text{ min}$ , reaching a primary peak of approximately  $12.8 \text{ m s}^{-1}$  at  $-72 \text{ min}$  (Fig. 8d), coinciding with a secondary peak in LLJ frequency. Following a brief weakening ( $-60$  to  $-48 \text{ min}$ ), a renewed and explosive intensification occurred from  $-48 \text{ min}$  onwards, continuing until rainfall onset. Throughout this period, the LLJ cores remained concentrated between  $0.5$ – $1.5 \text{ km a.g.l.}$  (Fig. 7d). In sharp contrast, LLJ\_non-HR events displayed a pattern of premature peaking followed by decay. Both frequency and intensity peaked earlier at  $-84 \text{ min}$ , fol-

lowed by general attenuation (Fig. 7h). By  $-48 \text{ min}$ , weakened wind profiles stabilized into a double-core structure maintaining around  $10 \text{ m s}^{-1}$ , with distinct jet cores near  $0.8 \text{ km}$  and  $1.7 \text{ km a.g.l.}$  (Fig. 8h). Crucially, in the LLJ\_non-HR event, this premature peak and the subsequent continuous attenuation of the low-level wind field resulted in a lack of sustained dynamic forcing during the critical pre-rainstorm stage, failing to trigger HR.

Synthesizing the evolution across all phases, although a distinct transient weakening of the jet profile was consistently observed, LLJs exhibited a rapid re-intensification of wind speed accompanied by a lowering of the jet core height

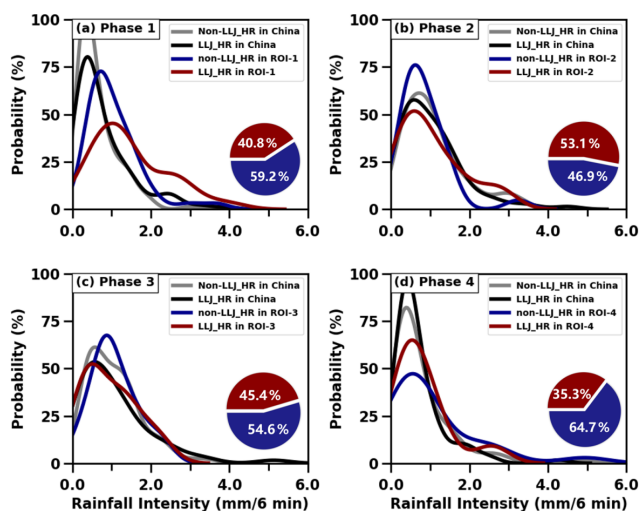


**Figure 6.** (a) Probability density distributions of average rain rate ( $\text{mm } 6 \text{ min}^{-1}$ ) for LLJ\_HR events (black solid lines) and non-LLJ\_HR events (gray solid lines) across China during Phase 1, and specifically in ROI-1 for LLJ\_HR events (red solid lines) and non-LLJ\_HR events (blue solid lines). (b–d) the same as panel (a), but for comparisons between national-scale and other regional-scale events in ROI-2 during Phase 2, ROI-3 during Phase 3, and ROI-4 during Phase 4. The pie chart at the lower right shows the proportion distribution of LLJ\_HR (red) and non-LLJ\_HR (blue) events in these key regions during each period.

during approximately the final 30 min preceding HR. This recurring pre-rainfall adjustment suggests that LLJs underwent a short-term dynamical reorganization prior to HR onset. We propose that this minute-scale oscillatory behavior – characterized by a “weakening-then-strengthening” or “descent-then-ascent” pattern – constitutes a robust dynamic precursor of HR. Physically, the temporary weakening may reflect momentum redistribution or enhanced turbulent mixing, whereas the subsequent intensification and descent of the jet core likely enhance low-level moisture convergence and vertical wind shear, thereby strengthening upward motion and promoting convective development (Markowski and Richardson, 2011). Such rapid structural adjustment indicates that the timing and vertical evolution of LLJs, rather than their mere presence, play a critical role in modulating heavy rainfall production.

Furthermore, probability distributions of LLJ strength and height within 2 h preceding rainfall were compared across key regions (Fig. 9). During Phase 1 in ROI-1, the strength of LLJs in LLJ\_HR events was notably stronger by 2–3  $\text{m s}^{-1}$  than that in LLJ\_non-HR events (Fig. 9a). Height distributions showed distinct bimodal peaks near 0.9 km and 1.75 km a.g.l. (Fig. 9e). The average LLJs height was generally higher in LLJ\_HR events, which is usually affected by the coupling of the upper-level jet stream or the land-sea breeze. During Phase 2 in ROI-2, LLJ\_HR events showed higher probabilities of strong LLJs (17–28  $\text{m s}^{-1}$ ) compared

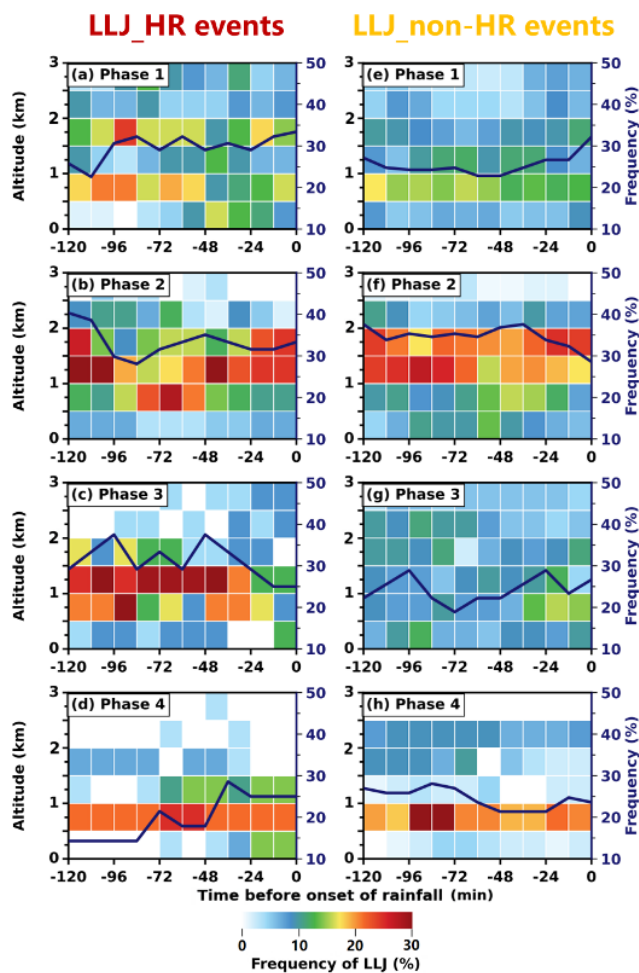


**Figure 7.** Time-height evolution of LLJ occurrence frequency (color shading, every 12 min, within 500 m vertical bins) detected by RWP with 2 h preceding nocturnal rainfall in LLJ\_HR events in (a) ROI-1 during Phase 1, (b) ROI-2 during Phase 2, (c) ROI-3 during Phase 3, and (d) in ROI-4 during Phase 4. Dark blue solid lines denote accumulated LLJ frequency over 0–3 km latitude. (e–h) Same as (a–d), but for LLJ\_non-HR events.

to the dominant 13  $\text{m s}^{-1}$  intensity in LLJ\_non-HR events (Fig. 9b). Influenced by large-scale circulation patterns, both event types featured LLJs centered near 1.5 km a.g.l. (Fig. 9f), though LLJ\_HR events developed a secondary maximum near 0.8 km a.g.l. due to pre-rainfall descent of the jet core (Fig. 7b). Contrastingly, Fig. 9c shows that LLJ\_HR events were associated with weaker jet strengths (around 11  $\text{m s}^{-1}$ ) compared to LLJ\_non-HR events (14–23  $\text{m s}^{-1}$ ) in ROI-3 during Phase 3, suggesting that strong LLJs do not necessarily induce HR here. The height of LLJ in LLJ\_HR events mainly concentrated near 1.2 km a.g.l., whereas in LLJ\_non-HR events, it was more uniformly distributed between 0–3 km a.g.l. with a higher probability nearly 1.5 km (Fig. 9g). For Phase 4 in ROI-4, LLJs strength peaked near 15  $\text{m s}^{-1}$  in both event types, but LLJ\_HR events fea-

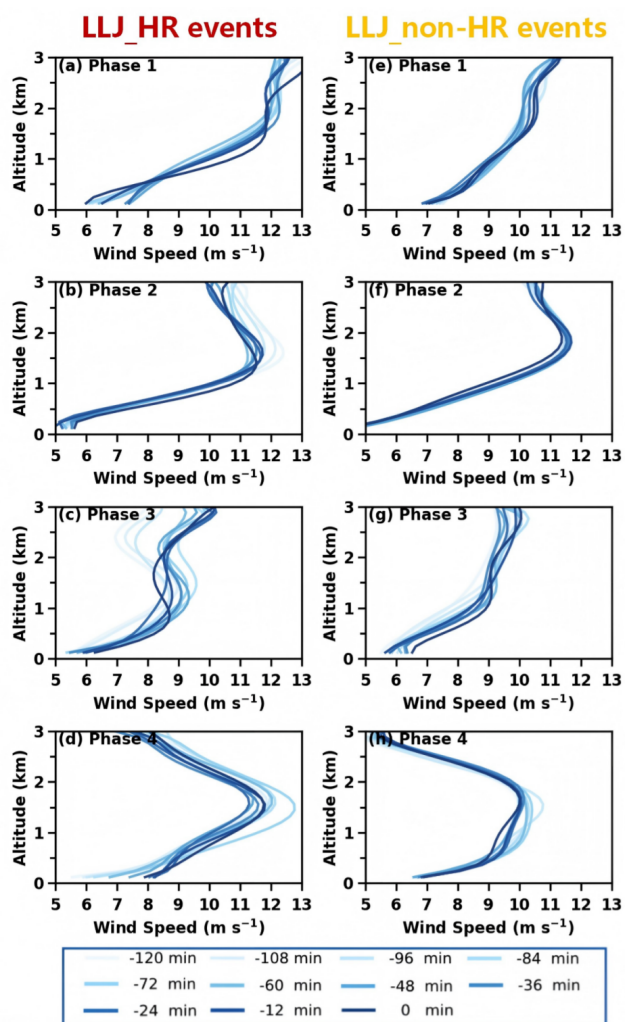


**Figure 8.** (a–d) Evolution of RWP-detected mean wind profiles of LLJs (blue solid lines, every 12 min) within 2 h preceding nocturnal rainfall in LLJ\_HR events in (a) ROI-1 during Phase 1, (b) ROI-2 during Phase 2, (c) ROI-3 during Phase 3, and (d) in ROI-4 during Phase 4. (e–h) Same as (a–d), but for LLJ\_non-HR events.

tured stronger jets reaching 25–30 m s<sup>-1</sup> (Fig. 9d). The LLJs height in both events peaked predominantly at 0.8 km a.g.l., with secondary peaks at 1.5 km for LLJ\_HR and 2.0 km a.g.l. for LLJ\_non-HR events (Fig. 9h).

In summary, although different internal dynamic adjustments, including frequency, occurrence height, and wind profile intensity of LLJs, preceding LLJ\_HR events were observed due to the different dominant mechanisms influencing rainfall in each phase, our findings highlight the role of fine-scale LLJ structures and their rapid vertical reorganization in modulating nocturnal rainfall intensity, offering valuable insights for improving regional nocturnal HR forecasting.

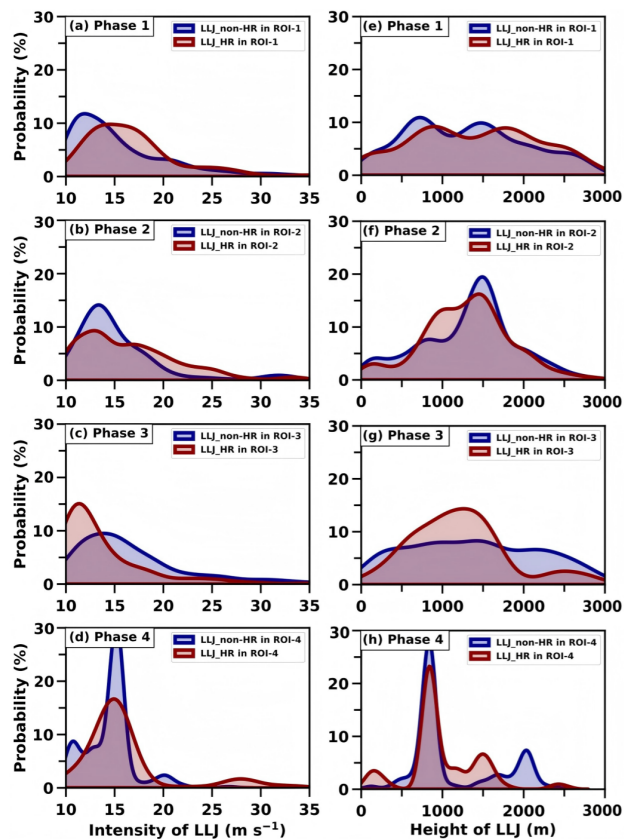


**Figure 9.** Probability density distributions of jet core intensity from RWP observations within 2 h preceding nocturnal rainfall in LLJ\_HR events in (a) ROI-1 during Phase 1, (b) ROI-2 during Phase 2, (c) ROI-3 during Phase 3, and (d) in ROI-4 during Phase 4. (e–h) Same as (a–d), but for the height of LLJs.

### 3.3 Thermodynamic evolution associated with LLJs preceding nocturnal heavy and non-heavy Rainfall

The Sect. 3.2 has clarified that the fine-scale dynamic characteristics of LLJs – including their temporal evolution, vertical structure and intensity variations – play a pivotal role in modulating nocturnal rainfall intensity during rainy season phases. However, the influence of LLJs on rainfall generation and intensification rarely operates in isolation; instead, it depends strongly on the accompanying large-scale thermodynamic environment, which provides the necessary moisture supply and convective instability to sustain or amplify heavy rainfall. Thus, to fully unravel the mechanisms underlying the distinction between LLJ\_HR and LLJ\_non-HR events, it is essential to complement the dynamic analysis with an in-depth examination of the thermodynamic conditions associated with LLJs within the immediate pre-convective environment (within 1-h preceding rainfall).

Further analysis of the large-scale thermodynamic conditions at 1 h prior to rainfall onset (Figs. 10 and 11) reveals consistently stronger thermal instability for LLJ\_HR versus

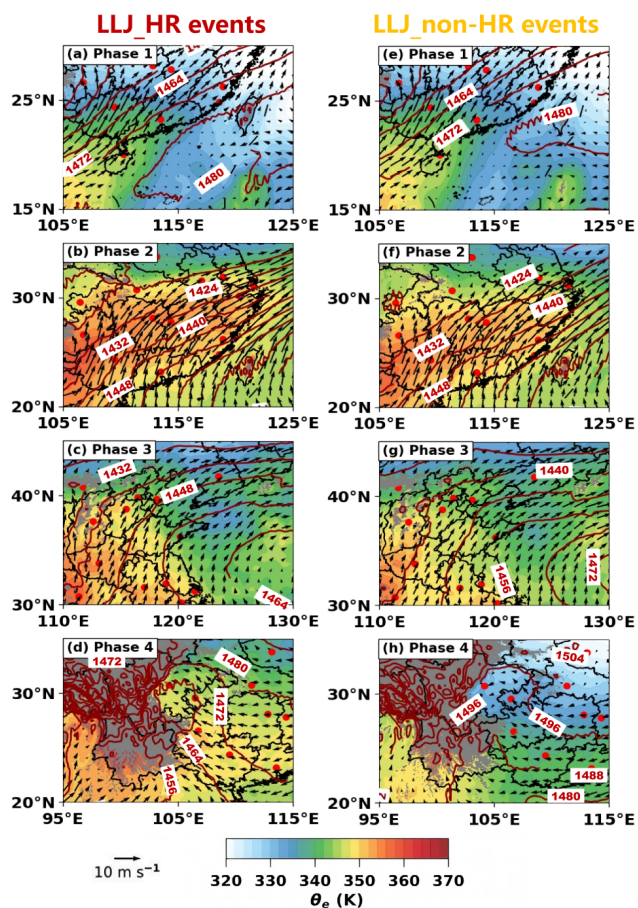


**Figure 10.** Distributions of equivalent potential temperature (shading, unit: K) at 850 hPa, superimposed with 850 hPa horizontal wind vectors (black arrows) and geopotential height contours (red solid lines), for LLJ\_HR events within 1-h time window preceding nocturnal rainfall onset in (a) ROI-1 during Phase 1, (b) ROI-2 during Phase 2, (c) ROI-3 during Phase 3, and (d) in ROI-4 during Phase 4. Gray shading denotes terrain elevation exceeding 850 hPa level. The reference vector ( $10 \text{ m s}^{-1}$ ) is shown at the lower-left corner. (e–h) Same as (a–d), but for LLJ\_non-HR events.

LLJ\_non-HR events, accompanied by stronger MFC within key regions during each rainy season.

During Phase 1 in ROI-1, thermodynamic conditions were comparable between event types. Southwesterly LLJs transported warm-moist air masses from the South China Sea and Bay of Bengal, forming a pronounced warm-humid tongue (Fig. 10a and e). Coupled with MFC centers developing north of the jet axis (Fig. 11a and e), this configuration facilitated nocturnal rainfall development. During Phase 2 in ROI-2, LLJ\_HR events exhibited a significantly stronger warm-moisture tongue with core  $\theta_e$  reaching 358 K – approximately 2 K higher than in non-HR events (Fig. 10b and f). Dynamically, the stronger LLJ core (difference  $> 1.2 \text{ m s}^{-1}$ ) drove a sharper, continuous band of MFC along the left flank of the jet axis (Fig. 11b), creating a ro-

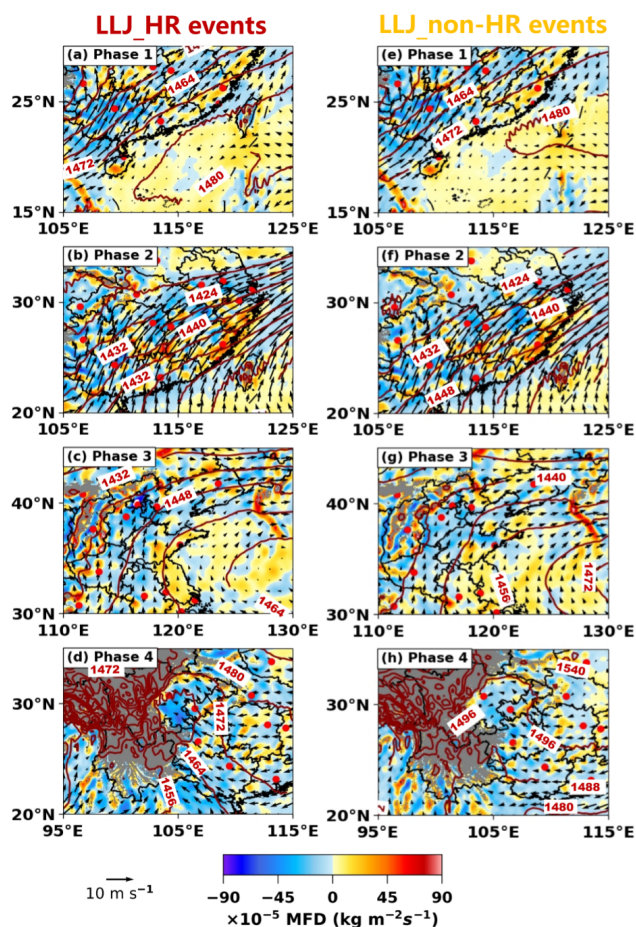


**Figure 11.** Same as Fig. 10, but showing the integrated moisture flux divergence (shading, unit:  $\text{kg m}^{-2} \text{ s}^{-1}$ ) between 1000–700 hPa at 1 h prior to preceding nocturnal rainfall onset.

bust triggering mechanism for HR (Fig. 11b). During Phase 3 in ROI-3, intensified southwesterly LLJs in HR events drove substantial northward transport of abundant moisture and higher  $\theta_e$  air (difference  $> 2 \text{ K}$ ) northward into a low  $\theta_e$  environment (Fig. 10c), enhancing convective instability. The synergistic interaction of this moist, high-energy advection with orographic forcing from the Taihang Mountains generated intense MFC, with peak values south of Beijing approximately  $30 \times 10^{-5} \text{ kg m}^{-2} \text{ s}^{-1}$  (Fig. 11c) larger than those in LLJ\_non-HR events, thereby driving nocturnal HR. Thermodynamic contrasts were most pronounced during Phase 4 in ROI-4. Thermodynamic contrasts were most pronounced during Phase 4 in ROI-4. LLJ\_HR events featured a deep high- $\theta_e$  region ( $> 356 \text{ K}$ ) over the southeastern Tibetan Plateau (Fig. 10d), contrasting with the cold highs located to the northeast of ROI-4 and lower  $\theta_e$  prevalent in LLJ\_non-HR events (Fig. 10h). Concurrently, accelerated easterly-southeasterly LLJs drove warm, moist air towards the steep eastern Plateau margin. The impingement of this flow against the sharp topographic gradient generated intense

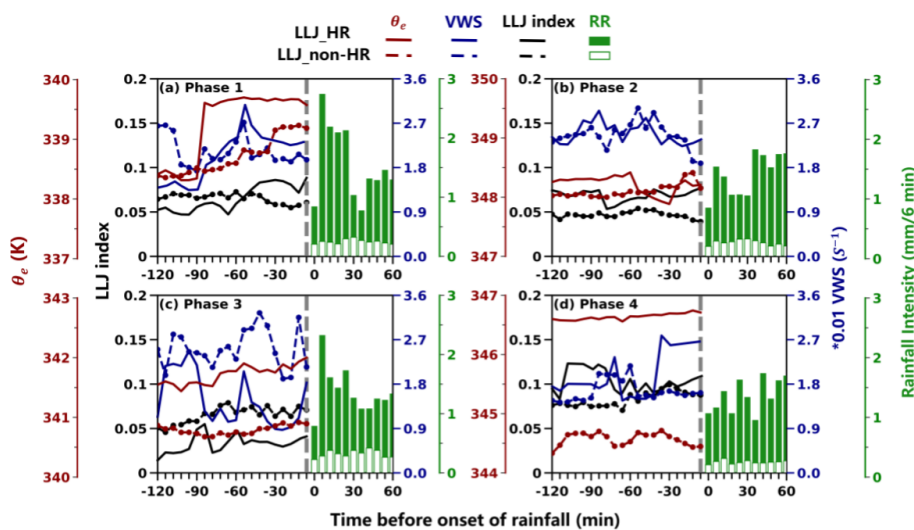


**Figure 12.** Temporal evolution of surface equivalent potential temperature ( $\theta_e$ , red lines), vertical wind shear (VWS, blue lines), and LLJ index (black lines) averaged within 2 h preceding nocturnal rainfall for LLJ\_HR events (solid lines) and LLJ\_non-HR events (dashed lines) in (a) ROI-1 during Phase 1, (b) ROI-2 during Phase 2, (c) ROI-3 during Phase 3, and (d) in ROI-4 during Phase 4. Green bars denote 6-min averaged rain rate ( $\text{mm } 6 \text{ min}^{-1}$ ) after LLJ\_HR (solid bars) and LLJ\_non-HR (open bars) events onset.

dynamic lifting and low-level convergence. This mechanically forced ascent, synergizing with the abundant moisture transport and strong MFC (Fig. 11h), played an essential role in triggering the observed nocturnal HR in this region.

To elucidate the rapid processes leading to occurrence of rainfall, the minute-scale evolution of key thermodynamic and dynamic parameters was further analyzed (Fig. 12), including surface  $\theta_e$ , LLJ index and VWS. Specifically, LLJ index is defined as the ratio of maximum wind speed below 3 km to the height where wind first exceeds  $10 \text{ m s}^{-1}$ . A rapid rise in LLJ index will reflect the extension and pulsing intensity of the LLJ, and its magnitude has been shown to be positively correlated with subsequent rainfall intensity 1–2 h later (Liu et al., 2003). VWS is calculated as the wind speed difference between the surface and jet height divided by the jet height and is used to characterize the bulk shear from the surface to the jet layer associated with the dynamical forcing and organization of convection (Wei et al., 2014).

Figure 12a illustrated that during Phase 1 in ROI-1, despite the similarity in large-scale environments between LLJ\_HR and LLJ\_non-HR events, they exhibited distinct differences in the continuous evolution of LLJ-associated thermodynamic conditions preceding rainfall onset. LLJ\_HR events exhibited abrupt thermodynamic enhancement from 90 min preceding the onset of rainfall driven by rapid intensification of LLJs, with surface  $\theta_e$  and VWS surging approximately  $1.5 \text{ K}$  and  $0.005 \text{ s}^{-1}$  respectively. Concurrently, the LLJ index surged from approximately 0.05 to 0.08 and VWS peaked sharply at  $-60 \text{ min}$ , signaling LLJs intensification and core descent (Figs. 7a, 8a). This rapid, minute-scale co-intensification of thermodynamic and dynamic processes serves as a critical precursor triggering HR. In con-

trast, LLJ\_non-HR events showed weaker increases of  $\theta_e$  and VWS and a declining LLJ index (by about 0.02) alongside rising jet cores, reducing low-level shear and convergence efficiency, thereby diminishing overall rainfall intensity.

During Phase 2 in ROI-2, the thermodynamic environment displayed a distinct “weakening-reintensification” pattern (Fig. 12b), which aligns precisely with the intrinsic dynamical adjustments of the wind field presented in Fig. 8b. Initially, at  $-120 \text{ min}$ , concurrent peaks in the LLJ index and VWS were observed, coupled with a high surface  $\theta_e$  of  $348.3 \text{ K}$ . During the subsequent transition period, a drastic elevation in the jet core height starting from  $-84 \text{ min}$  caused a precipitous drop in the LLJ index. The timing of this rapid evolution suggests a transient optimal window for nocturnal rainfall triggering that is characteristic of LLJ\_HR events in ROI-2. Following this, rapid surface cooling began 60 min prior to HR. This cooling was likely induced by the cold pool outflows associated with alternation or propagation of convective systems embedded within the Mei-Yu front cloud system (Zhang et al., 2023). The resulting dense cold air wedging beneath the strong southwesterly LLJs can lift the jet axis above the coldpool interface, further enhancing uplift and promoting rainfall (Luo et al., 2014). This in turn facilitated the final re-intensification of the jet structure (Figs. 7b and 8b). Crucially, this reorganized configuration sharply enhances lowlevel vertical wind shear and horizontal convergence (Fig. 12b), further promoting HR development. In contrast, LLJ\_non-HR events exhibited weaker thermodynamic support and diminished dynamic forcing with consistently lower LLJ indices within 60 min preceding rainfall, resulting in insufficient lift to sustain HR. Compared with the disordered fluctuations of the LLJ\_non-HR events, LLJ\_HR

events highlight the importance of thermal-dynamic synergy influenced by LLJs evolution. Even though the LLJ evolution may be modulated by convective feedback, the resulting reorganized jet profile still can serve as a robust dynamical precursor essential for triggering local HR.

During Phase 3 in ROI-3, LLJ\_HR events featured prominent thermal compensation (surface  $\Delta\theta_e > 1$  K, 850 hPa  $\Delta\theta_e > 2$  K versus non-HR events) – despite possessing generally weaker dynamical forcing compared to other phases (Fig. 12c). Temporally, the evolution was marked by distinct pulsations: The LLJ index exhibited a rapid rise (from  $\sim 0.03$  to  $\sim 0.06$ ) starting 84 min prior to HR onset (Fig. 12c) driven by a surge of LLJs profiles, while VWS peaked synchronously with the maximum LLJ frequency. Subsequently, a secondary peak in both the LLJ index and VWS was observed between  $-60$  and  $-48$  min. Although the subsequent declines in wind speed and frequency led to notable fluctuations in these parameters, the VWS and LLJ index underwent substantial intensification (with VWS increasing by  $\sim 1.5$  s $^{-1}$ ) in the final 24 min, driven by the rapid acceleration of the LLJ wind field. This co-evolution with rapid surface warming (increase of 0.25 K) released convective instability and enhanced convergence (Fig. 10). Nevertheless, the overall weaker dynamical conditions likely limited the depth and organization of convection, potentially accounting for the reduced probability of heavier rainfall compared to other phases. In contrast, during LLJ non-HR events, the LLJ index ( $\sim 0.03$ ) and  $\theta_e$  vary rather gradually.

During Phase 4 in ROI-4, under the favorably thermal environments ( $\theta_e > 346$  K), LLJ\_HR events showed a two-stage dynamic intensification. Initially, the LLJ index surged, while the VWS and jet intensity reached synchronous secondary peaks at  $-72$  min. In the second stage, VWS increased rapidly by  $\sim 0.9$  (Fig. 12d), and the LLJ index maintained an overall upward trend, peaking immediately prior to onset due to the surging jet. But LLJ\_non-HR events showed weakening trends in both dynamic and thermodynamic conditions during the final 30 min and exhibited weaker changes ( $\Delta$ VWS  $< 0.45$  s $^{-1}$ ,  $\Delta$ LLJ index  $< 0.02$ ), reflecting an absence of the coordinated intensification necessary to initiate and sustain HR.

Although the evolution paths of the thermodynamic environment vary across different phases, a universal cross-region precursor emerges: the LLJ index and VWS consistently exhibits a strengthening or stabilizing trend in the final approximately 30 min preceding HR onset, operating in concert with significant low-level warming (rising  $\theta_e$ ). In contrast, non-HR events generally lack this culminating dynamical intensification. Overall, these results adequately showcase the sensitivity of regional HR to the fine-scale structural evolution of LLJs and their coupling with thermodynamic environments.

## 4 Summary and concluding remarks

Using wind profile measurements from a nationwide network of 31 RWP during the warm seasons (April–October) of 2023–2024, this study characterized the minute-scale evolution of LLJs as dynamic precursors to nocturnal rainfall across China. By systematically comparing the vertically resolved structure and temporal evolution of LLJs within the 2-h window preceding nocturnal HR and non-HR events across four distinct rainy-season phases, we identified the key dynamic-thermodynamic distinctions governing rainfall intensity.

At the national scale, nocturnal rainfall accounted for nearly half of the total warm-season precipitation, and 56 % of nocturnal rainfall events were preceded by LLJs within 2 h. In the key regions of interest (ROIs), approximately 45.0 % of identified HR events were associated with LLJs. Overall, LLJ-related events were significantly more prone to producing heavier rainfall than non-LLJ events across most regions, underscoring the strong coupling between LLJs and nocturnal HR.

Despite regional differences in synoptic forcing, consistent contrast in LLJ evolution were observed between HR and non-HR events across all phases. During Phase 1 in ROI-1, a bimodal vertical distribution of LLJs and their rapid thermodynamic-dynamic co-intensification starting 84 min prior to rainfall were identified as key precursors of LLJ\_HR events, in sharp contrast to the decoupled dynamics of LLJ\_non-HR events. Phase 2 (ROI-2) was characterized by a distinct oscillatory process, where HR events featured a rapid descent of the LLJ core below 1 km followed by a robust rebound, distinguishing them from the quasi-steady state of LLJ\_non-HR cases. In Phase 3 (ROI-3), LLJ\_HR events exhibited significant thermal compensation and bimodal pulsations (peaks at  $-96$  and  $-48$  min), with a critical final-stage intensification serving as the decisive trigger. Similarly, Phase 4 (ROI-4) featured a distinctive two-stage intensification, where a rapid LLJ surge within 48 min of onset distinguished LLJ\_HR events from the significantly attenuated dynamical structures of LLJ\_non-HR events.

Although the detailed dynamical pathways vary among phases, a unifying feature emerges: all LLJ\_HR events exhibit a “final-stage intensification” of low-level dynamics – manifested as enhanced LLJ strength, vertical wind shear, and LLJ index – within approximately 30 min preceding rainfall, occurring in synergy with increasing thermodynamic instability (e.g., rising equivalent potential temperature,  $\theta_e$ ). This result confirms the universality of the final-stage low-level dynamic amplification identified in our previous study (Li et al., 2024) and demonstrates its national-scale applicability across diverse monsoon regimes.

Crucially, this study further identifies a previously under-resolved “preparatory adjustment” phase occurring 30–120 min prior to rainfall onset, during which LLJ frequency, strength and core height undergo systematic minute-scale re-

organization. This national-scale evidence indicates that the final dynamic trigger is contingent upon this earlier synergistic coupling of minute-scale jet structural evolution and thermodynamic destabilization. This rapid, synergistic reorganization represents a necessary precondition for HR generation and contrasts sharply with the comparatively steady evolution observed in LLJ\_non-HR events. These results highlight that the occurrence and intensity of nocturnal rainfall are governed not simply by LLJ presence, but by the fine-scale vertical evolution of LLJs and their interaction with regional thermodynamic conditions.

Overall, this study establishes robust dynamic-rainfall linkages associated with LLJs across different warm-season rainy periods in China. Future research should: (1) expand multi-source observations to establish dynamic thresholds for early forecasting systems of nocturnal rainfall, and (2) develop quantitative frameworks relating LLJ structural evolution to rainfall intensity, offering theoretical support for optimizing physical processes in LLJ parameterization schemes within high-resolution numerical models. Further investigation is also needed to clarify the physical mechanisms controlling rapid adjustments in LLJ core height and strength immediately prior to rainfall onset.

**Data availability.** The LLJs retrieved from the RWP network can be acquired from <https://doi.org/10.5281/zenodo.17176759> (Li and Guo, 2025). The data from the weather station are obtained from the China Meteorological Data Service Centre at <https://data.cma.cn/en> (last access: 1 March 2026), and the original ERA5 reanalysis data used here are available from the ECMWF in Hersbach et al. (2023).

**Supplement.** The supplement related to this article is available online at <https://doi.org/10.5194/acp-26-3339-2026-supplement>.

**Author contributions.** The study was completed with close cooperation between all authors. JG designed the research framework; NL performed the analysis and drafted the original manuscript with contribution from JG; JG, XG, ZZ, YZ, JG, NT, YW, and YZ helped revise the manuscript.

**Competing interests.** The contact author has declared that none of the authors has any competing interests.

**Disclaimer.** Publisher's note: Copernicus Publications remains neutral with regard to jurisdictional claims made in the text, published maps, institutional affiliations, or any other geographical representation in this paper. The authors bear the ultimate responsibility for providing appropriate place names. Views expressed in the text are those of the authors and do not necessarily reflect the views of the publisher.

**Acknowledgements.** We appreciate tremendously the constructive comments and suggestions made by the editor and two anonymous reviewers that significantly improved the quality of our manuscript.

**Financial support.** This research has been supported by the National Natural Science Foundation of China (grant no. 42325501), the Science and Technology Supporting Project of Guizhou Province (grant no. [2023]236) and the National Key Research and Development Program of China (grant no. 2024YFC3013001).

**Review statement.** This paper was edited by Bingbing Wang and reviewed by two anonymous referees.

## References

- Anthes, R. A., Kuo, Y. H., Benjamin, S. G., and Li, Y. F.: The evolution of the mesoscale environment of severe local storms: Preliminary modeling results, *Mon. Weather Rev.*, 110, 1187–1213, [https://doi.org/10.1175/1520-0493\(1982\)110<1187:TEOTME>2.0.CO;2](https://doi.org/10.1175/1520-0493(1982)110<1187:TEOTME>2.0.CO;2), 1982.
- Bai, L., Chen, G., Huang, Y., and Meng, Z.: Convection initiation at a coastal rainfall hotspot in South China: Synoptic patterns and orographic effects, *J. Geophys. Res.-Atmos.*, 126, e2021JD034642, <https://doi.org/10.1029/2021JD034642>, 2021.
- Blackadar, A. K.: Boundary layer wind maxima and their significance for the growth of nocturnal inversions, *Bull. Am. Meteorol. Soc.*, 38, 283–290, <https://doi.org/10.1175/1520-0477-38.5.283>, 1957.
- Bonner, W. D.: Climatology of the low-level jet, *Mon. Weather Rev.*, 96, 833–850, [https://doi.org/10.1175/1520-0493\(1968\)096<0833:COTLLJ>2.0.CO;2](https://doi.org/10.1175/1520-0493(1968)096<0833:COTLLJ>2.0.CO;2), 1968.
- Cao, Q., Guo, J., Xue, C., Li, Z., Xu, H., Li, N., Sun, Y., Zhang, Z., Wang, Y., Chen, J., Zhou, Y., and Chen, T.: Divergent Sounding-derived Precursor Pathways Enable Discrimination of Dry versus Wet Severe Convective Winds, *Geophys. Res. Lett.*, 52, e2025GL117491, <https://doi.org/10.1029/2025GL117491>, 2025.
- Carbone, R. E. and Tuttle, J. D.: Rainfall occurrence in the US warm season: The diurnal cycle, *J. Clim.*, 21, 4132–4146, <https://doi.org/10.1175/2008JCLI2275.1>, 2008.
- Chen, G., Sha, W., Iwasaki, T., and Wen, Z.: Diurnal Cycle of a Heavy Rainfall Corridor over East Asia, *Mon. Weather Rev.*, 145, 3365–3389, <https://doi.org/10.1175/mwr-d-16-0423.1>, 2017.
- Chen, H., Zhou, T., Neale, R. B., Wu, X., and Zhang, G. J.: Performance of the new NCAR CAM3. 5 in East Asian summer monsoon simulations: Sensitivity to modifications of the convection scheme, *J. Clim.*, 23, 3657–3675, <https://doi.org/10.1175/2010JCLI3022.1>, 2010.
- Chen, T., Guo, J., Guo, X., Zhang, Y., Xu, H., and Zhang, D.-L.: On the multiscale processes leading to an extreme gust wind event in East China: Insights from radar wind profiler mesonet observations, *J. Geophys. Res.-Atmos.*, 129, e2024JD041484, <https://doi.org/10.1029/2024JD041484>, 2024.
- Chen, X., Zhang, F., and Zhao, K.: Diurnal Variations of the Land-Sea Breeze and Its Related Precipitation over South China, *J.*

- Atmos. Sci., 73, 4793–4815, <https://doi.org/10.1175/JAS-D-16-0106.1>, 2016.
- China Meteorological Administration: Specification for Automatic Observation of Ground Meteorology, China Meteorological Press, <https://ncooc.121.com.cn/qhgx/annex/3/32/1200/2024030614361731.pdf> (last access: 28 February 2026), 2020.
- Davis, C. A., Maning, W. K., Carbone, R., Trier, S., and Tuttle, J.: Coherence of warm-season continental rainfall in numerical weather prediction models, *Mon. Weather Rev.*, 131, 2667–2679, [https://doi.org/10.1175/1520-0493\(2003\)131<2667:COWCRI>2.0.CO;2](https://doi.org/10.1175/1520-0493(2003)131<2667:COWCRI>2.0.CO;2), 2003.
- Dong, F., Zhi, X., Zhang, L., and Ye, C.: Diurnal variations of coastal boundary layer jets over the northern South China Sea and their impacts on diurnal cycle of rainfall over southern China during the early-summer rainy season, *Mon. Weather Rev.*, 149, 3341–3363, <https://doi.org/10.1175/MWR-D-20-0292.1>, 2021.
- Doubler, D. L., Winkler, J. A., Bian, X., Walters, C. K., and Zhong, S.: An NARR-derived climatology of southerly and northerly low-level jets over North America and coastal environs, *J. Appl. Meteorol. Climatol.*, 54, 1596–1619, <https://doi.org/10.1175/JAMC-D-14-0311.1>, 2015.
- Du, Y. and Chen, G.: Heavy Rainfall Associated with Double Low-Level Jets over Southern China. Part I: Ensemble-Based Analysis, *Mon. Weather Rev.*, 146, 3827–3844, <https://doi.org/10.1175/MWR-D-18-0101.1>, 2018.
- Du, Y. and Chen, G.: Heavy Rainfall Associated with Double Low-Level Jets over Southern China. Part II: Convection Initiation, *Mon. Weather Rev.*, 147, 543–565, <https://doi.org/10.1175/mwr-d-18-0102.1>, 2019.
- Du, Y., Zhang, Q., Ying, Y., and Yang, Y.: Characteristics of low-level jets in Shanghai during the 2008–2009 warm seasons as inferred from wind profiler radar data, *J. Meteorol. Soc. Jpn. Ser. II*, 90, 891–903, <https://doi.org/10.2151/jmsj.2012-603>, 2012.
- Du, Y., Zhang, Q., Chen, Y., Zhao, Y., and Wang, X.: Numerical simulations of spatial distributions and diurnal variations of low-level jets in China during early summer, *J. Clim.*, 27, 5747–5767, <https://doi.org/10.1175/JCLI-D-13-00571.1>, 2014.
- Du, Y., Chen, G., Han, B., Bai, L., and Li, M.: Convection initiation and growth at the coast of South China. Part II: Effects of the terrain, coastline, and cold pools, *Mon. Weather Rev.*, 148, 3871–3892, <https://doi.org/10.1175/MWR-D-20-0090.1>, 2020.
- Fu, S. M., Jin, S. L., Shen, W., Li, D. Y., Liu, B., and Sun, J. H.: A kinetic energy budget on the severe wind production that causes a serious state grid failure in Southern Xinjiang China, *Atmos. Sci. Lett.*, 21, e977, <https://doi.org/10.1002/asl.977>, 2020.
- Gebauer, J. G., Shapiro, A., Fedorovich, E., and Klein, P.: Convection Initiation Caused by Heterogeneous Low-Level Jets over the Great Plains, *Mon. Weather Rev.*, 146, 2615–2637, <https://doi.org/10.1175/mwr-d-18-0002.1>, 2018.
- Guo, X., Guo, J., Zhang, D. L., and Yun, Y.: Vertical divergence profiles as detected by two wind-profiler mesonets over East China: Implications for nowcasting convective storms, *Q. J. R. Meteorol. Soc.*, 149, 1629–1649, <https://doi.org/10.1002/qj.4474>, 2023.
- Hersbach, H., Bell, B., Berrisford, P., Biavati, G., Horányi, A., Muñoz Sabater, J., Nicolas, J., Peubey, C., Radu, R., Rozum, I., Schepers, D., Simmons, A., Soci, C., Dee, D., and Thépaut, J.-N.: ERA5 hourly data on pressure levels from 1940 to present. Copernicus Climate Change Service (C3S) Climate Data Store (CDS), <https://doi.org/10.24381/cds.bd0915c6>, 2023.
- Higgins, R. W., Yao, Y., Yarosh, E. S., Janowiak, J. E., and Mo, K. C.: Influence of the Great Plains low-level jet on summertime precipitation and moisture transport over the central United States, *J. Clim.*, 10, 481–507, 1997.
- Hodges, D. and Pu, Z.: Characteristics and Variations of Low-Level Jets and Environmental Factors Associated with Summer Precipitation Extremes over the Great Plains, *J. Clim.*, 32, 5123–5144, <https://doi.org/10.1175/JCLI-D-18-0553.1>, 2019.
- Holton, J. R.: The diurnal boundary layer wind oscillation above sloping terrain, *Tellus*, 19, 200–205, <https://doi.org/10.3402/tellusa.v19i2.9766>, 1967.
- Horinouchi, T., Matsumura, S., Ose, T., and Takayabu, Y. N.: Jet-precipitation relation and future change of the mei-yu-baiu rainband and subtropical jet in CMIP5 coupled GCM simulations, *J. Clim.*, 32, 2247–2259, <https://doi.org/10.1175/JCLI-D-18-0426.1>, 2019.
- Huang, X., Sun, J., and Liu, W.: The interaction between low-level jet evolution and severe convective rainstorms under topographic effect, *Acta Meteorol. Sin.*, 78, 551–567, 2020.
- Li, N. and Guo, J.: Data for wind profiles associated with LLJs obtained from RWP observations during the warm season (April–October) of 2023–2024 in China, Zenodo [data set], <https://doi.org/10.5281/zenodo.17176759>, 2025.
- Li, N., Guo, J., Wu, M., Zhang, F., Guo, X., Sun, Y., Zhang, Z., Liang, L., and Chen, T.: Low-level jet and its effect on the onset of summertime nocturnal rainfall in Beijing, *Geophys. Res. Lett.*, 51, e2024GL110840, <https://doi.org/10.1029/2024GL110840>, 2024.
- Li, X. and Du, Y.: Statistical relationships between two types of heavy rainfall and low-level jets in South China, *J. Clim.*, 34, 8549–8566, <https://doi.org/10.1175/JCLI-D-21-0121.1>, 2021.
- Liu, B., Ma, Y., Guo, J., and Wei, G.: Boundary layer heights as derived from ground-based radar wind profiler in Beijing, *IEEE Trans. Geosci. Remote Sens.*, 57, 8095–8104, <https://doi.org/10.1109/TGRS.2019.2918301>, 2019.
- Liu, S., Zheng, Y., and Tao, Z.: The analysis of the relationship between pulse of LLJ and heavy rain using wind profiler data, *J. Trop. Meteorol.*, 2, 158–163, 2003 (in Chinese).
- Liu, X., Luo, Y., Huang, L., Zhang, D. L., and Guan, Z.: Roles of double low-level jets in the generation of coexisting inland and coastal heavy rainfall over south China during the presummer rainy season, *J. Geophys. Res.-Atmos.*, 125, e2020JD032890, <https://doi.org/10.1029/2020JD032890>, 2020.
- Luo, Y., Gong, Y., and Zhang, D. L.: Initiation and organizational modes of an extreme-rain-producing mesoscale convective system along a mei-yu front in East China, *Mon. Weather Rev.*, 142, 203–221, <https://doi.org/10.1175/MWR-D-13-00111.1>, 2014.
- Maddox, R. A.: Large-scale meteorological conditions associated with midlatitude, mesoscale convective complexes, *Mon. Weather Rev.*, 111, 1475–1493, 1983.
- Maddox, R. A. and Doswell III, C. A.: An examination of jet stream configurations, 500 mb vorticity advection and low-level thermal advection patterns during extended periods of intense convection, *Mon. Weather Rev.*, 110, 184–197, [https://doi.org/10.1175/1520-0493\(1982\)110<0184:AEJSC>2.0.CO;2](https://doi.org/10.1175/1520-0493(1982)110<0184:AEJSC>2.0.CO;2), 1982.

- Marengo, J. A., Soares, W. R., Saulo, C., and Nicolini, M.: Climatology of the low-level jet east of the Andes as derived from the NCEP-NCAR reanalyses: Characteristics and temporal variability, *J. Clim.*, 17, 2261–2280, 2004.
- Markowski, P. and Richardson, Y.: *Mesoscale meteorology in midlatitudes*, John Wiley & Sons, <https://doi.org/10.1002/9780470682104>, 2011.
- Miao, Y., Guo, J., Liu, S., Wei, W., Zhang, G., Lin, Y., and Zhai, P.: The Climatology of Low-Level Jet in Beijing and Guangzhou, China, *J. Geophys. Res.-Atmos.*, 123, 2816–2830, <https://doi.org/10.1002/2017jd027321>, 2018.
- Mitchell, M. J., Arritt, R. W., and Labas, K.: A climatology of the warm season Great Plains low-level jet using wind profiler observations, *Weather Forecast.*, 10, 576–591, 1995.
- Molod, A., Salmun, H., and Collow, A. B. M.: Annual cycle of planetary boundary layer heights estimated from wind profiler network data, *J. Geophys. Res.-Atmos.*, 124, 6207–6221, <https://doi.org/10.1029/2018JD030102>, 2019.
- Monaghan, A. J., Rife, D. L., Pinto, J. O., Davis, C. A., and Hannan, J. R.: Global precipitation extremes associated with diurnally varying low-level jets, *J. Clim.*, 23, 5065–5084, 2010.
- Pan, H. and Chen, G.: Diurnal variations of precipitation over North China regulated by the mountain-plains solenoid and boundary-layer inertial oscillation, *Adv. Atmos. Sci.*, 36, 863–884, <https://doi.org/10.1175/2010JCLI3515.1>, 2019.
- Pitchford, K. L. and London, J.: The low-level jet as related to nocturnal thunderstorms over Midwest United States, *J. Appl. Meteorol.*, 1, 43–47, 1962.
- Rasmusson, E. M.: Atmospheric water vapor transport and the water balance of North America. Part I: Characteristics of the water vapor flux field, *Mon. Weather Rev.*, 95, 403–426, [https://doi.org/10.1175/1520-0493\(1967\)095,0403:AWVTAT.2.3.CO;2](https://doi.org/10.1175/1520-0493(1967)095<0403:AWVTAT.2.3.CO;2), 1967.
- Rasmussen, K. L. and Houze Jr, R. A.: Convective initiation near the Andes in subtropical South America, *Mon. Weather Rev.*, 144, 2351–2374, <https://doi.org/10.1175/MWR-D-15-0058.1>, 2016.
- Reif, D. Q. and Bluestein, H.: A 20-year climatology of nocturnal convection initiation over the central and southern great plains during the warm season, *Mon. Weather Rev.*, 145, 1615–1639, <https://doi.org/10.1175/MWR-D-16-0340.1>, 2017.
- Roots, M., Sullivan, J. T., and Demoz, B.: Mid-Atlantic nocturnal low-level jet characteristics: a machine learning analysis of radar wind profiles, *Atmos. Meas. Tech.*, 18, 1269–1282, <https://doi.org/10.5194/amt-18-1269-2025>, 2025.
- Stensrud, D. J.: Importance of low-level jets to climate: A review, *J. Clim.*, 9, 1698–1711, 1996.
- Subrahmayam, K. V., Udupa, S. R., Kumar, K. K., Ramana, M. V., Srinivasulu, J., and Bothale, R. V.: Prediction of zonal wind using machine learning algorithms: Implications to future projections of Indian monsoon jets, *J. Indian Soc. Remote Sens.*, 52, 371–381, 2024.
- Sun, S. Q., Zhai, G. H., and Lorenzo, D. O.: The relationship between large-scale low-level jet over east asia and monsoon as well as cross-equatorial currents in summer, *Acta Meteorol. Sin.*, 1, 43–50, 1986.
- Trier, S. B., Wilson, J. W., Ahijevych, D. A., and Sobash, R. A.: Mesoscale vertical motions near nocturnal convection initiation in PECAN, *Mon. Weather Rev.*, 145, 2919–2941, <https://doi.org/10.1175/MWR-D-17-0005.1>, 2017.
- Trier, S. B., Davis, C. A., Ahijevych, D. A., Weisman, M. L., and Bryan, G. H.: Mechanisms supporting long-lived episodes of propagating nocturnal convection within a 7-day WRF model simulation, *J. Atmos. Sci.*, 63, 2437–2461, <https://doi.org/10.1175/JAS3768.1>, 2006.
- Tuttle, J. D. and Davis, C. A.: Corridors of warm season precipitation in the central United States, *Mon. Weather Rev.*, 134, 2297–2317, <https://doi.org/10.1175/MWR3188.1>, 2006.
- Uccellini, L. W. and Johnson, D. R.: The coupling of upper and lower tropospheric jet streaks and implications for the development of severe convective storms, *Mon. Weather Rev.*, 107, 682–703, [https://doi.org/10.1175/1520-0493\(1979\)107<0682:TCOUAL>2.0.CO;2](https://doi.org/10.1175/1520-0493(1979)107<0682:TCOUAL>2.0.CO;2), 1979.
- Walters, C. K., Winkler, J. A., Shadbolt, R. P., van Ravensway, J., and Bierly, G. D.: A long-term climatology of southerly and northerly low-level jets for the central United States, *Ann. Assoc. Am. Geogr.*, 98, 521–552, 2008.
- Wang, D., Zhang, Y., and Huang, A.: Climatic features of the southwesterly low-level jet over southeast China and its association with precipitation over east China, Asia-Pac, *J. Atmos. Sci.*, 49, 259–270, <https://doi.org/10.1007/s13143-013-0025-y>, 2013.
- Weckwerth, T. M. and Wakimoto, R. M.: The initiation and organization of convective cells atop a cold-air outflow boundary, *Mon. Weather Rev.*, 120, 2169–2187, [https://doi.org/10.1175/1520-0493\(1992\)120<2169:TIAOOC>2.0.CO;2](https://doi.org/10.1175/1520-0493(1992)120<2169:TIAOOC>2.0.CO;2), 1992.
- Weckwerth, T. M., Hanesiak, J., Wilson, J. W., Trier, S. B., Degelia, S. K., Gallus Jr, W. A., Roberts, R. D., and Wang, X.: Nocturnal convection initiation during PECAN 2015, *Bull. Am. Meteorol. Soc.*, 100, 2223–2239, <https://doi.org/10.1175/BAMS-D-18-0299.1>, 2019.
- Wei, W., Zhang, H. S., and Ye, X. X.: Comparison of low-level jets along the north coast of China in summer, *J. Geophys. Res.-Atmos.*, 119, 9692–9706, <https://doi.org/10.1002/2014jd021476>, 2014.
- Weisman, M. L., Trapp, R. J., Romine, G. S., Davis, C., Torn, R., Baldwin, M., Bosart, L., Brown, J., Coniglio, M., Dowell, D., Evans, A. C., Galarneau, T. J., Haggerty, J., Hock, T., Manning, K., Roebber, P., Romashkin, P., Schumacher, R., Schwartz, C. S., Sobash, R., Stensrud, D., and Trier, S. B.: The mesoscale predictability experiment (MPEX), *Bull. Am. Meteorol. Soc.*, 96, 2127–2149, <https://doi.org/10.1175/bams-d-13-00281.1>, 2015.
- Whiteman, C. D., Bian, X., and Zhong, S.: Low-level jet climatology from enhanced Rawinsonde observations at a site in the southern Great Plains, *J. Appl. Meteorol.*, 36, 1363–1376, [https://doi.org/10.1175/1520-0450\(1997\)036<1363:LLJCFE>2.0.CO;2](https://doi.org/10.1175/1520-0450(1997)036<1363:LLJCFE>2.0.CO;2), 1997.
- Xia, R. and Zhao, S.: Diagnosis and modeling of meso-scale systems of heavy rainfall in warm sector ahead of front in South China (middle part of Guangdong province) in June 2005, *Chin. J. Atmos. Sci.*, 33, <https://doi.org/10.3878/j.issn.1006-9895.2009.03.06>, 2009.
- Xue, M., Luo, X., Zhu, K., Sun, Z., and Fei, J.: The controlling role of boundary layer inertial oscillations in Meiyu frontal precipitation and its diurnal cycles over China, *J. Geophys. Res.-Atmos.*, 123, 5090–5115, <https://doi.org/10.1029/2018JD028368>, 2018.
- Yan, Y., Cai, X., Wang, X., Miao, Y., and Song, Y.: Low-level jet climatology of China derived from long-term radiosonde observations, *J. Geophys. Res.-Atmos.*, 126, e2021JD035323, <https://doi.org/10.1029/2021JD035323>, 2021.

- Yu, R., Li, J., Chen, H., and Yuan, W.: Progress in studies of the precipitation diurnal variation over contiguous China, *J. Meteorol. Res.*, 28, 877–902, <https://doi.org/10.1007/s13351-014-3272-7>, 2014.
- Zamora, R. J., Shapiro, M. A., and Doswell III., C. A.: The diagnosis of upper tropospheric divergence and ageostrophic wind using profiler wind observations, *Mon. Weather Rev.*, 115, 871–884, [https://doi.org/10.1175/1520-0493\(1987\)115<0871:TDOUTD>2.0.CO;2](https://doi.org/10.1175/1520-0493(1987)115<0871:TDOUTD>2.0.CO;2), 1987.
- Zhang, F., Zhang, Q., Sun, J., and Xu, J.: Convection initiation during the Meiyu environment in the Yangtze-Huai River basin of China, *J. Geophys. Res.-Atmos.*, 128, e2022JD038077, <https://doi.org/10.1029/2022JD038077>, 2023.
- Zhang, M. and Meng, Z.: Warm-sector heavy rainfall in southern China and its WRF simulation evaluation: A low-level-jet perspective, *Mon. Weather Rev.*, 147, 4461–4480, <https://doi.org/10.1175/MWR-D-19-0110.1>, 2019.
- Zhang, Y., Xue, M., Zhu, K., and Zhou, B.: What is the main cause of diurnal variation and nocturnal peak of summer precipitation in Sichuan Basin, China? the key role of boundary layer low-level jet inertial oscillations, *J. Geophys. Res.-Atmos.*, 124, 2643–2664, <https://doi.org/10.1029/2018jd029834>, 2019.
- Zhao, Y., Liao, J., Zhang, Q., Chen, J., Gong, X., Shi, Y., Shi, M., Yang, D., Fan, S., Zhou, X., Cao, L., and Hu, K.: Development of China Ground Climate Normal Value Dataset from 1991 to 2020, *Chin. J. Atmos. Sci.*, 48, 555–571, <https://doi.org/10.3878/j.issn.1006-9895.2204.22010>, 2024 (in Chinese).